The 5th Joint International Conference on Multibody System Dynamics
June 24 – 28, 2018, Lisboa, Portugal

Coupling Multibody and Granular Dynamics: Experimental Validation

Olivier Lantsoght[1], Paul Fisette[1], Frédéric Dubois[2], Olivier Brüls[3] and Nicolas Docquier[1]

[1]*Institute of Mechanics, Materials, and Civil Engineering (iMMC), Université catholique de Louvain (UCL)*
[2]*LMGC, Univ. Montpellier, CNRS, Montpellier, France*
[3]*Department of Aerospace and Mechanical Engineering, University of Liège*

ABSTRACT — *Multibody systems can interact with other systems or with the environment via contacts. Such interactions can be solved by different techniques such as the co-simulation process, or a monolithic solver. In some fields of application specific treatments are needed for example when the contacts are stiff and numerous, and when vibrations dramatically impact the behavior of one system. For these applications, dedicated solving strategies have to be applied. To check the coherence of such strategy with the real process, we developed an experimental setup involving a multibody system blending a granular media. The proposed planar experiment consists of a modified four-bar linkage blending a set of disks contained in a vibrating box shaked at different frequencies. The experiment measures the interactions between both systems at different frequencies via a telescopic bar included in the four-bar linkage.*

1 Introduction

Many engineering applications involve a mechanical articulated system interacting with granular media such as the transportation of granular material, the displacement of a vehicle on gravel or the mixing of powder. In particular our research project focuses on the tamping process of railway ballast. This maintenance operation of railway track consists in restoring the track geometry by squeezing the ballast grains located under the sleepers. The particularity of this process is to take advantage of the ability of the granular media to behave like a fluid in order to reduce the loads during the tamping process. To reach this state of fluidification, the granular material has to be excited in a specific frequency range. Our developments were focused on simulating such problems. For this purpose, we couple the multibody system (MBS) dynamics approach with the discrete element method (DEM) using non-smooth contact dynamics .

The high contact stiffness of the ballast has motivated our choice of using NSCD. We can cite Flores et al. [1] that extended the approach of Jean [2] to unconstrained MBS and Acary and Brogliato [3] who describe several methods for non-smooth dynamical systems. A non-smooth generalized-α scheme, which enables to enforce the unilateral constraints both at position and velocity levels for frictionless contact, has been proposed by Brüls and al. [4]. The main particularity of our work [5] lays in the way we combine bilateral and unilateral constraints in the solver. We provide the contact solver - based on a non-smooth Gauss-Seidel procedure - with all the frictional contact constrains underlying the bilateral ones. This is achieved thanks to the coordinate partitioning method inspired for Wehage and Haug [6]. This particularity ensures that the solution of the frictional contact constraints fulfills bilateral ones coming from the MBS. Thanks to that, we are able to solve problems involving a lots of contacts (granular media) with very low cpu overheating due to the bilateral constraints.

To compare numerical strategies coupling non-smooth contacts and MBS, several numerical benchmarks have been previously proposed, as, for example, the woodpecker toy introduced by Pfeiffer and Glocker [7] or the slider-crank mechanism proposed by Flores et al. [1]. These benchmarks are useful to check resolution schemes when they deal with contact between different bodies of the MBS (ex: gap in joints). Our benchmark is designed to

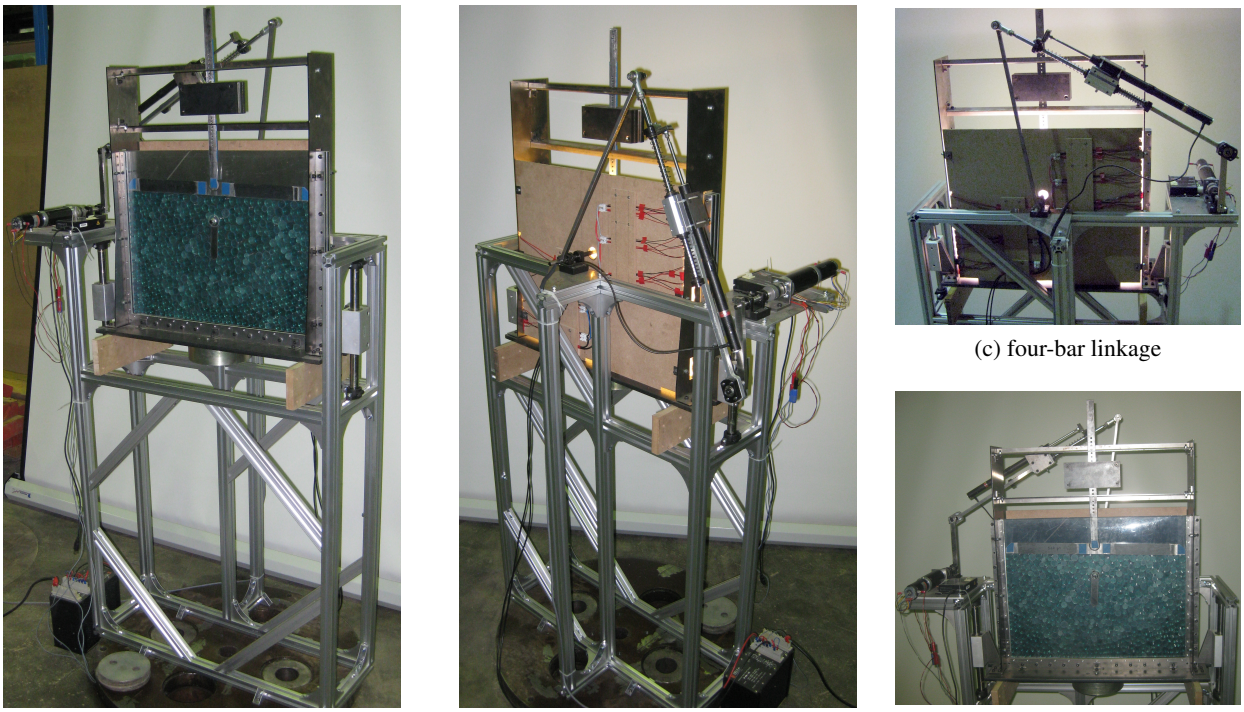

(a) Front view (b) Back view (c) four-bar linkage (d) Granular media

Fig. 1: Experimental set-up in laboratory without the hydraulic actuator

compare numerical methods dedicated to interaction between granular media and MBS. Such are able to capture specific granular media behavior - like the fluidisation phenomena - and the corresponding reaction on the MBS. For this benchmark we have developed a specific experiment (Fig 1) that will allow to validate our modeling work.

This paper will be divided in three main sections. The first one briefly describes the methodology we developed. The second section is dedicated to the full description of the experimental setup. Finally the last section presents the actual results but also discusses further analyses to be done.

2 Methodology

To model the target applications, MBS dynamics is coupled with the DEM, the first being suited to describe articulated mechanisms while the latter is dedicated to granular media. In this paper we only give a short summary of the key elements of the methodology we used for the numerical simulation. Another paper describing the whole methodology is being written.

Contact dynamics The contact dynamic model is an approach based on non-smooth contact laws which prevent bodies from interpenetration. The equation in the normal direction of contact reads:

$$\text{if } g \leq 0 \text{ then } V_{\hat{n}} \geq 0,\ R_{\hat{n}} \geq 0,\ V_{\hat{n}}\, R_{\hat{n}} = 0 \tag{1}$$

where g is the gap, $V_{\hat{n}}$ and $R_{\hat{n}}$ are the normal component of the relative velocity and of the reaction force between the two bodies. In the tangential direction a Coulomb friction law is used:

$$\begin{aligned} &\text{if } g \leq 0: \\ &\qquad \text{if } \|\mathbf{V}_{\hat{\mathbf{t}}}\| = 0 \quad \text{then } \|\mathbf{R}_{\hat{\mathbf{t}}}\| \leq \mu R_{\hat{n}} \\ &\qquad \text{if } \|\mathbf{V}_{\hat{\mathbf{t}}}\| \neq 0 \quad \text{then } \mathbf{R}_{\hat{\mathbf{t}}} = -\mu R_{\hat{n}} \frac{\mathbf{V}_{\hat{\mathbf{t}}}}{\|\mathbf{V}_{\hat{\mathbf{t}}}\|} \end{aligned} \tag{2}$$

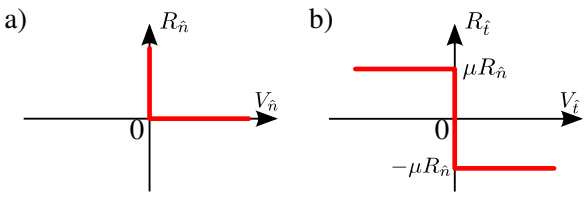

Fig. 2: Contact force: a) Signorini's condition in normal direction b) Coulomb's condition in tangential direction

where μ is the friction coefficient, $\mathbf{V}_{\hat{\mathbf{t}}}$ and of the $\mathbf{R}_{\hat{\mathbf{t}}}$ are the tangential vector of the velocities and reaction force between the bodies. The equations (1) and (2) illustrated in figure 2, are referred as the "Signorini-Coulomb" condition.

A Newton impact law $V_{\hat{n}}^{+} = -eV_{\hat{n}}^{-}$ describes the dynamics of contact. The coefficient of restitution $e \in [0,1]$ and the superscripts $-$ and $+$ indicate the pre- and post-impact velocity. The non-smooth part of the dynamics is introduced by this law as the velocity field of bodies is no more continuous. As a consequence, the equations of motion are no more integrable using standard methods based on the knowledge of the accelerations.

Coupled equations of motion The coupling between DEM and MBS equations occurs in the contact conditions. The contacts introduce the unilateral constraints in both equations of motion. For the MBS, after applying the coordinate partitioning technique, [8], we obtain te reduce set of the equations of motion in term of independent generalized coordinate $\mathbf{q_u}$:

$$\mathbf{M_r}(\mathbf{q_u})d\dot{\mathbf{q}}_\mathbf{u} = \mathbf{F_r}(\mathbf{q_u},\dot{\mathbf{q}}_\mathbf{u})dt + \mathbf{H}_{\mathbf{r}mbs}(\mathbf{q_u},\mathbf{q}_{dem})\,d\mathbf{I}_{\mathscr{U}} \tag{3}$$

written in terms of differential measures of the independent velocities $d\dot{\mathbf{q}}_\mathbf{u}$. In this equation, $\mathbf{M_r}$ and $\mathbf{F_r}$ are the reduced mass matrix and the non linear dynamical vector coming from the coordinate partitioning ([8]) of the MBS. As regards the DEM equation of motion, they are also written in terms of differential measures of the velocities $d\dot{\mathbf{q}}_{dem}$:

$$\mathbf{M}_{dem}d\dot{\mathbf{q}}_{dem} = \mathbf{F}(\mathbf{q}_{dem},\dot{\mathbf{q}}_{dem})dt + \mathbf{H}_{dem}(\mathbf{q_u},\mathbf{q}_{dem})\,d\mathbf{I}_{\mathscr{U}} \tag{4}$$

Where $\mathbf{q}_{dem}$ denotes the granular media generalized coordinates and $\mathbf{F}(\mathbf{q}_{dem}$ is the non linear dynamical vector including the external forces and torques. In the equations (3) and (4)), $\mathbf{dI}_{\mathscr{U}}$ represents the differential measures of the contact reactions over the time step. The matrices $\mathbf{H}_{\mathbf{r}mbs}$ and $\mathbf{H}_{dem}$ are used to project these quantities, expressed in the contacts frame, in the coordinate system of each domain.

Coupled solution of the dynamics To solve the dynamics of those system, a time discretization inspired from the time stepping scheme of the Non-Smooth Contact Dynamics submitted by Moreau and Jean [2] is applied. This scheme express the contact dynamics in the contact frame:

$$\begin{array}{ll} \mathbf{V}_{n+1} = & \mathbf{V}_{free} + \mathbf{W}\,\mathbf{I}_{\mathscr{U}} \\ \text{with :} & \mathbf{V}_{free} = \mathbf{H}^{T}_{(\mathbf{q}_m)}\left(\dot{\mathbf{q}}_n + \mathbf{M}^{-1}_{(\mathbf{q}_m)}h\mathbf{F}_{(\mathbf{q}_m,\dot{\mathbf{q}}_n,t)}\right) \\ & \mathbf{W} = \mathbf{H}^{T}_{(\mathbf{q}_m)}\mathbf{M}_{(\mathbf{q}_m)}\mathbf{H}_{(\mathbf{q}_m)} \\ & \mathbf{q}_m = \mathbf{q}_n + (1-\theta)\,h\dot{\mathbf{q}}_n \end{array} \tag{5}$$

where $\mathbf{M}$ and $\mathbf{F}$ regroups the mass matrix and the force vector, of MBS and DEM. The matrix $\mathbf{H}$ is a concatenation of the matrices $\mathbf{H}_{\mathbf{r}mbs}$ and $\mathbf{H}_{dem}$. $\dot{\mathbf{q}}$ is the concatenation of $\dot{\mathbf{q}}_\mathbf{u}$ with $\dot{\mathbf{q}}_{dem}$ and $\mathbf{V}$ are the contact velocities expressed in they own frame. h is the time step and θ a parameter of the time integrator [2]. This problem is solved while satisfying the contact laws (1) and (2) with a Non-Linear Gauss-Seidel (NLGS) procedure. Full resolution of the contact dynamics is available in [2] and the explanation about the bilateral constraints respect is planned in another paper and will not be discussed here.

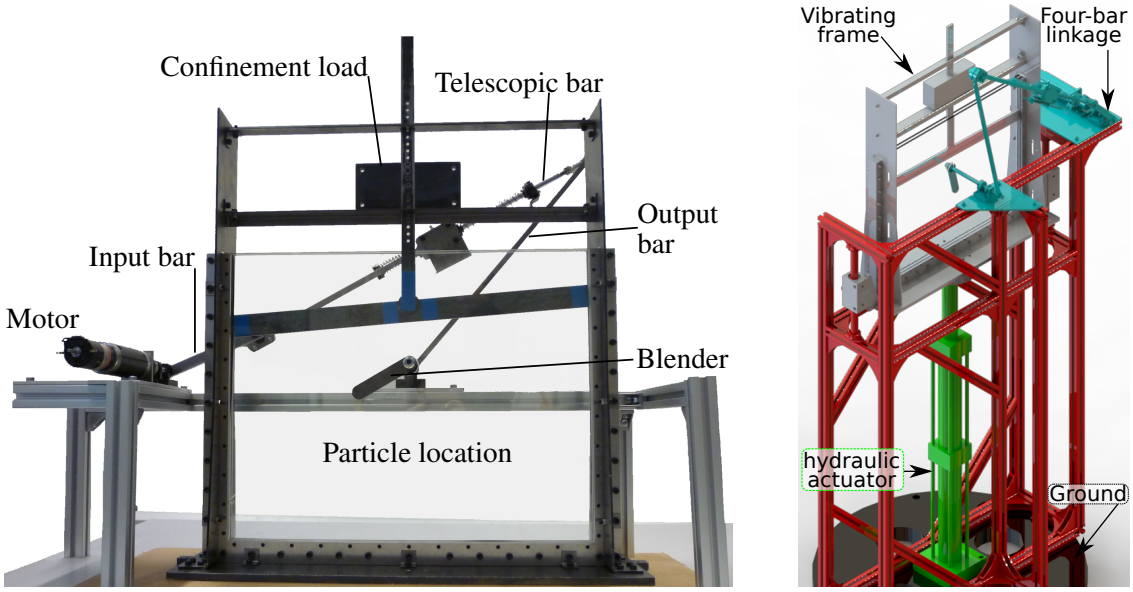

(a) Real set-up being assembled

(b) Final set-up rendering

Fig. 3: Experimental set-up: the four-bar linkage is fixed on the ground, the frame containing the granular media is shacked by an vertical hydraulic actuator.

3 Experimental setup

As previously said, the applications we are aiming to study are quite different from the numerical benchmark available in the literature such as the slider-crank mechanism with backslash. In the existing examples, NSCD is located in the MBS joints or between the MBS and a ground fixed wall. On the opposite, our applications involve a lot of contacts between free bodies (DEM approach) and only a few of them are in contact with a MBS. Moreover, the applications we aim to model take advantage of the ability of granular media to behave like a fluid while excited at specific vibration range. To check that our algorithm is able to capture such a phenomenon and to properly propagate the granular dynamics and to couple with multibody dynamics. We proposed in [10] to develop a benchmark based on numerical simulation. Now, we present the experimental setup that was designed from these numerical studies. This setup has been build and the analyses that we conducted on it are described in the following section.

The benchmark, rendered in fig. 3, is composed of 3 parts, detailed hereafter, interacting together via contacts.

1. a modified four-bar linkage, which blends the particles;
2. more than 500 cylindrical particles, representing the granular media;
3. a vibrating frame containing the particles, used to introduce vibrations in the media;

3.1 The four-bar linkage

A classical planar four-bar linkage has only one degree of freedom, usually actuated via one of the bars and whose resulting motion of another bar is used for the application at hand. In our benchmark we connected a DC-motor with constant controlled velocity on the input and a blender (a piece of metal) is interacting with the granular media at the other extremity, rigidly connected to the output bar (Fig 4). As the goal of this set-up is to observe the impact of the particles vibration on the four-bar linkage, we replaced the floating bar by a telescopic one. During the experiment a linear potentiometer measures the length of this telescopic bar.

In summary the modified planar four-bar linkage is a MBS composed of 4 bodies which are:

1. The input bar, connected to the DC-motor;
2. The telescopic bar made of two sliding bodies connected by two compression spring;
3. The output crank, rigidly linked with the blender;

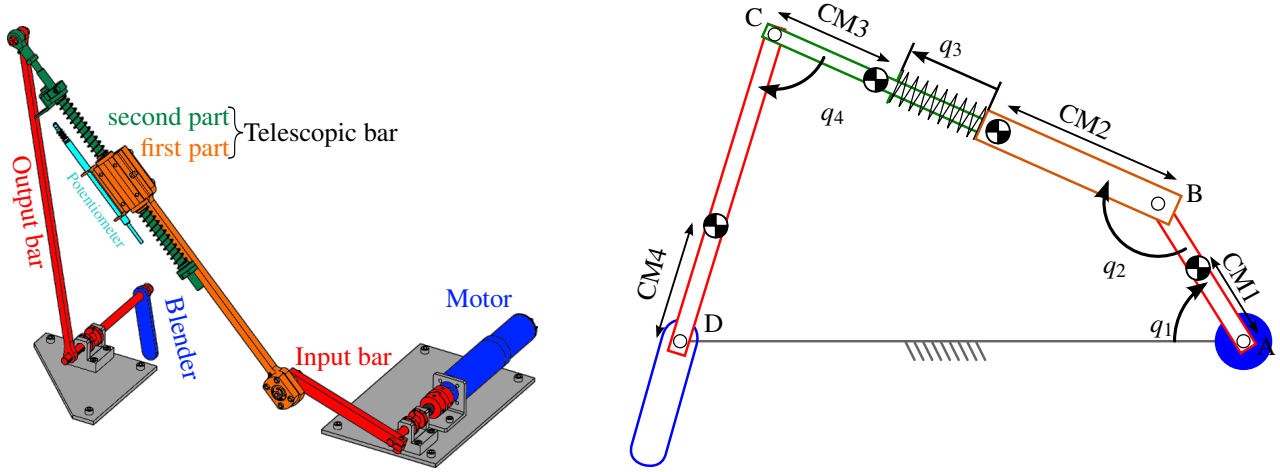

(a) 3D-rendering

(b) Sketche

Fig. 4: four-bar mechanism

Body name	mass	Inertia	Center of mass	Length
Input bar and axis	0.51 kg	1.6×10^{-3} kg m^2	CM1 = 40 mm	AB = 150 mm
Telescopic bar, first part	0.79 kg	15.4×10^{-3} kg m^2	CM2 = 258 mm	n/a
Telescopic bar, second part	0.34 kg	5.1×10^{-3} kg m^2	CM3 = 171 mm	n/a
Output bar and blender	0.50 kg	13.5×10^{-3} kg m^2	CM4 = 118 mm	CD = 450 mm
Base	n/a	n/a	n/a	AD = 450 mm

Tab. 1: Properties of the four-bar linkage

The kinematics of the mechanism and the useful data are given in Fig 4b and Tab 1. The parameters of the bodies are limited in 2D as we assume that the third dimension does not impact our results. The mass and inertia of the potentiometer has been included in the body it is attached to. All those values have been evaluated through a CAD representation of the system. The blender is a rectangle with semicircles at a pair of opposite sides, it's center of rotation being coincident with the center of the upper semicircle. The Fig 5 gives the dimensions while the thickness is 5 mm.

A regards the telescopic bar, the two compression springs (Fig 4a) do not always act together. Depending on the length of the bar only one spring may be under compression (while the other does not produce any force), or both springs work under compression. So the effective stiffness of the telescopic bar assembly is length dependent as illustrated in Fig 6a. The properties of the individual springs are given in Fig 6b.

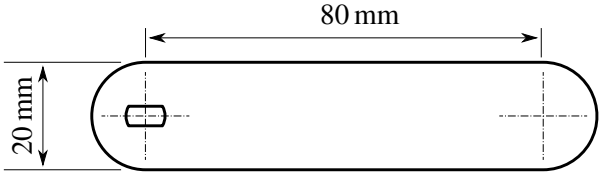

Fig. 5: Blender geometry

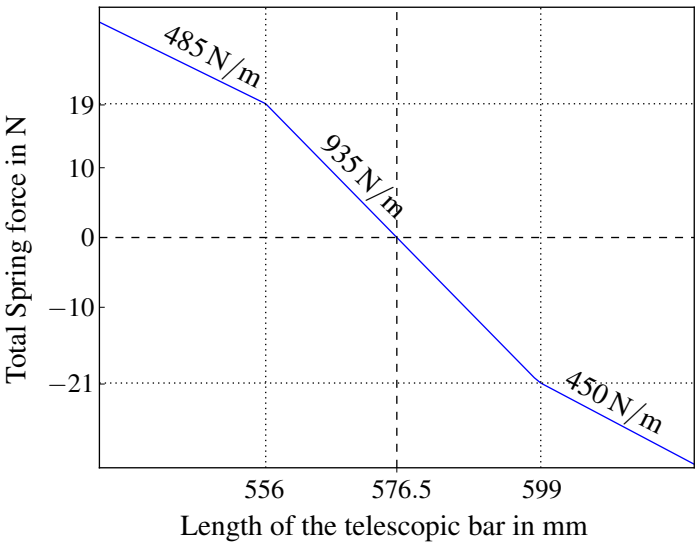

(a) Force applied by the spring

	Stiffness	Neutral length
Spring 1	485 N/m	93 mm
Spring 2	450 N/m	140 mm

(b) Physical properties of springs

Fig. 6: Details on the telescopic bar

Diameter	mass	Inertia	Nb particles	Mass proportion
12 mm	0.6 g	10.6 g mm^2	111	9.9 %
14 mm	0.8 g	19.6 g mm^2	126	15.1 %
16 mm	1.0 g	33.5 g mm^2	128	19.1 %
18 mm	1.3 g	53.6 g mm^2	117	22.7 %
20 mm	2.0 g	98.0 g mm^2	111	33.2 %

Tab. 2: Characteristics of the particles

3.2 Granular media

In the experiment, the granular media is a set of cylindrical particles (Fig 7a). To avoid locking phenomena in the media, there are 5 different cylinder sizes with diameters from 12 mm to 20 mm while their thickness is always 5 mm. The physical properties of the particles are given in Tab 2. The chosen material is the `Clear Flex`$^{\text{TM}}$`95` which is a clear urethane with a shore hardness about 95A and a density about 1040 kg m^{-3}. The particles were obtained by casting them into a metal mold with a free surface (Fig 7b). To avoid the natural cohesion between particles due to humidity, some talcum powder were applied on them.

The choice of the urethane for our particles is motivated by the birefringence (also called double refraction) of this material. This property causes to the incident light change of phase like in a waveplate. We take advantage of this property to capture the stress field in our granular material by including a circular polariscope (3.2.1) in our device. The relation between phase retardation and stress state is given by the stress-optic law which is, for a plane stress state:

$$\delta = \frac{2\pi}{\lambda} h C_\lambda \left(\sigma_1 - \sigma_2\right) \tag{6}$$

where h is the thickness of the specimen, C_λ is the stress-optic coefficient of the material usually dependent of the wavelength of light and $\sigma_{1,2}$ are the principal stress components. To limit the study to one wavelength, some green colorant has been introduced in the particles. So, we consider a unique stress-optic coefficient as only a narrow band of wavelength light is transmitted. The value of the stress optic coefficient has been roughly evaluated at 2.4×10^{-9} m^2/N. By including a polariscope in our setup we are able to visualize the stress in the particles. With an algorithm, a modification of the one provided by Daniels et al. [16], we can determine the force network in the granular media and consequently some other informations described in the results. Of course, the use of an urethane introduces a non-negligible elasticity on the granular media. The next points will briefly gives informations about

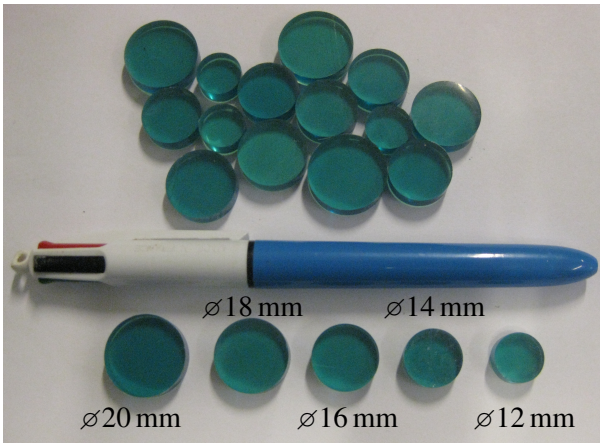

(a) Some particles

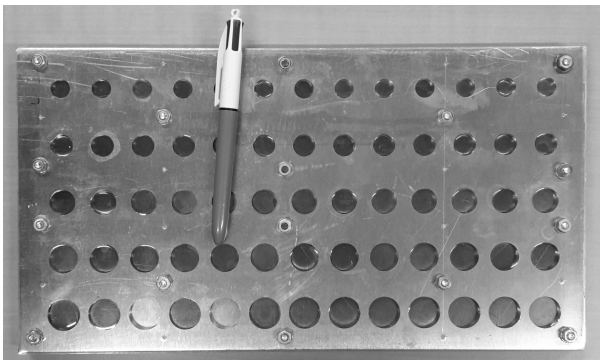

(b) Mold and particles

Fig. 7: Particles used in the experiment

the phenomena of photoelasticity.

3.2.1 photoelasticity

The photoelasticity refers to the variations of the optical properties of a material when submitted to deformation due to mechanical load. The method uses the property of some material to become birefringent when deformed and optically isotropic at rest. In the situation of planar stress and with the assumption of linear relationship between stress and strain, the two refractive indexes at each point of the material depend of the principal stress values and orientations. By selecting specific optical devices, this property can be exploited to experimentally observe the stress distribution inside a material. The so-called optical arrangement is called a polariscope. This section is mainly based on the publication of Ramesh [11], but numerous books detail this topic.

To express the visible light intensity in function of the stress state of the grains, we use the Jones calculus [12]. The Jones calculus deals with polarized light, expressed in the form of a complex vector. A plane monochromatic light linearly polarized along X axis and propagating along axis Z with Jones calculus is expressed by describing the electric field as

$$\begin{pmatrix} E_{x(t)} \\ E_{y(t)} \end{pmatrix} = \begin{pmatrix} 1 \\ 0 \end{pmatrix} k \exp(-i\omega t) \tag{7}$$

where k contains the information about intensity, ω is the circular velocity of light an t is the time. If the phase of the light along a component occurs, it will be stored in the complex multiplier: $\begin{pmatrix} 1\exp(i\phi) \\ 0 \end{pmatrix} k \exp(-i\omega t)$. But note that only the real part of the vector represent the physical electric field, the complex multiplier is only used to store the phase information of the electrical field.

The light intensity visible by the human eye is proportional to the multiplication of the electric field vector by its conjugate transpose. Moreover the time dependent variation is not considered as the light frequency (from 4×10^{14} Hz to 8×10^{14} Hz) is not detectable by optical sensor or human eye. So the equation of light intensity computed from the Jones vector is

$$I = \begin{pmatrix} E^{\star}_{x(t)} & E^{\star}_{y(t)} \end{pmatrix} \begin{pmatrix} E_{x(t)} \\ E_{y(t)} \end{pmatrix} k^2 \tag{8}$$

3.2.2 Circular polariscope

A circular polariscope is a setup that reveals the stresses in the studied model made of photoelastic material. The principle of this polariscope consists in transmitting circularly polarized light to the model, and pass refracted light through another circular polarizer called the analyzer. A circular polarizer is the combination of a linear polarizer

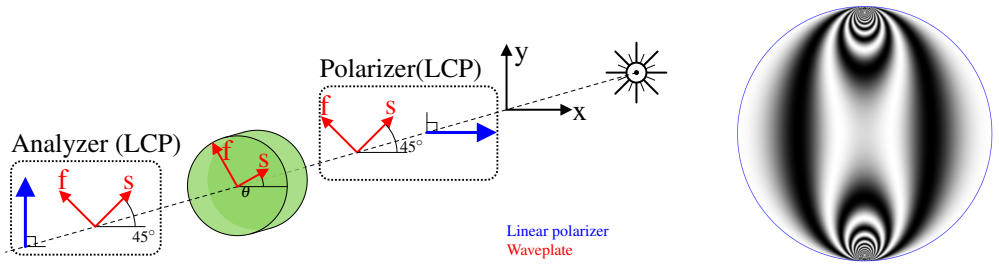

(a) Polariscope arrangement

(b) Result of a disk under radial compression

Fig. 8: Bright-field circular polariscope used in the experiment

placed before a quarter-waveplate oriented at $\pi/4$. The arrangement that we use (Fig 8a) is composed of two left-handed circular polarizer. The result is a bright-field polariscope, meaning that the background is clear. Other arrangements are possible: a dark-field polariscope can be achieved by using a left-handed and a right-handed circular polarizer.

To determine the light at any point of the specimen, we use the Jones calculus. Starting from the Jones vector of a linearly polarized light along x-axis given at equation (7), the setup is the multiplication of this vector by the Jones matrices corresponding to:

- a quarter-waveplate forming an angle $\theta = \pi/4$ with the linear polarizer to complete our left-handed polarizer.
- a waveplate, representing our specimen made of birefringent material; polarization axis and retardation values of the waveplate will rely on the stress state of the specimen.
- a quarter-waveplate forming an angle $\theta = \pi/4$ with the linear polarizer, with the next element it will represent our analyzer (a LCP).
- a linear filter with polarization axis aligned with y-axis.

As the Jones matrix of a general waveplate is

$$\begin{bmatrix} \cos\frac{\delta}{2} - i\sin\frac{\delta}{2}\cos 2\theta & -i\sin\frac{\delta}{2}\sin 2\theta \\ -i\sin\frac{\delta}{2}\sin 2\theta & \cos\frac{\delta}{2} + i\sin\frac{\delta}{2}\cos 2\theta \end{bmatrix} \tag{9}$$

and as a quarter-waveplate is obtained by substituting δ by $\pi/2$ in the previous equation we get

$$\begin{aligned} \begin{pmatrix} E_x \\ E_y \end{pmatrix} &= \begin{bmatrix} 0 & 0 \\ 0 & 1 \end{bmatrix} \frac{1}{\sqrt{2}} \begin{bmatrix} 1 & -i \\ -i & 1 \end{bmatrix} \begin{bmatrix} \cos\frac{\delta}{2} - i\sin\frac{\delta}{2}\cos 2\theta & -i\sin\frac{\delta}{2}\sin 2\theta \\ -i\sin\frac{\delta}{2}\sin 2\theta & \cos\frac{\delta}{2} + i\sin\frac{\delta}{2}\cos 2\theta \end{bmatrix} \frac{1}{\sqrt{2}} \begin{bmatrix} 1 & -i \\ -i & 1 \end{bmatrix} \begin{bmatrix} 1 \\ 0 \end{bmatrix} k\exp(-i\omega t) \\ &= \begin{bmatrix} 0 \\ -i\cos\frac{\delta}{2} \end{bmatrix} k\exp(-i\omega t) \end{aligned} \tag{10}$$

which is the equation of a circular polariscope arrangement. The visible light intensity at each point of the specimen is computed by applying the equation (8) to the Jones vector of the light refracted by the polariscope (eq:CircPol). The resulting light intensity is:

$$I = k^2\cos^2(\delta/2) \tag{11}$$

which means that we will only get full light extinction when $\delta = (2n+1)\pi$ with $n \in \mathbb{N}$. These fringes are called isochromatics (Fig 8b). As the stress-optic law (Eq 6) gives the value of retardation as a function of the principal stress value, we can link the visible intensity to the stress.

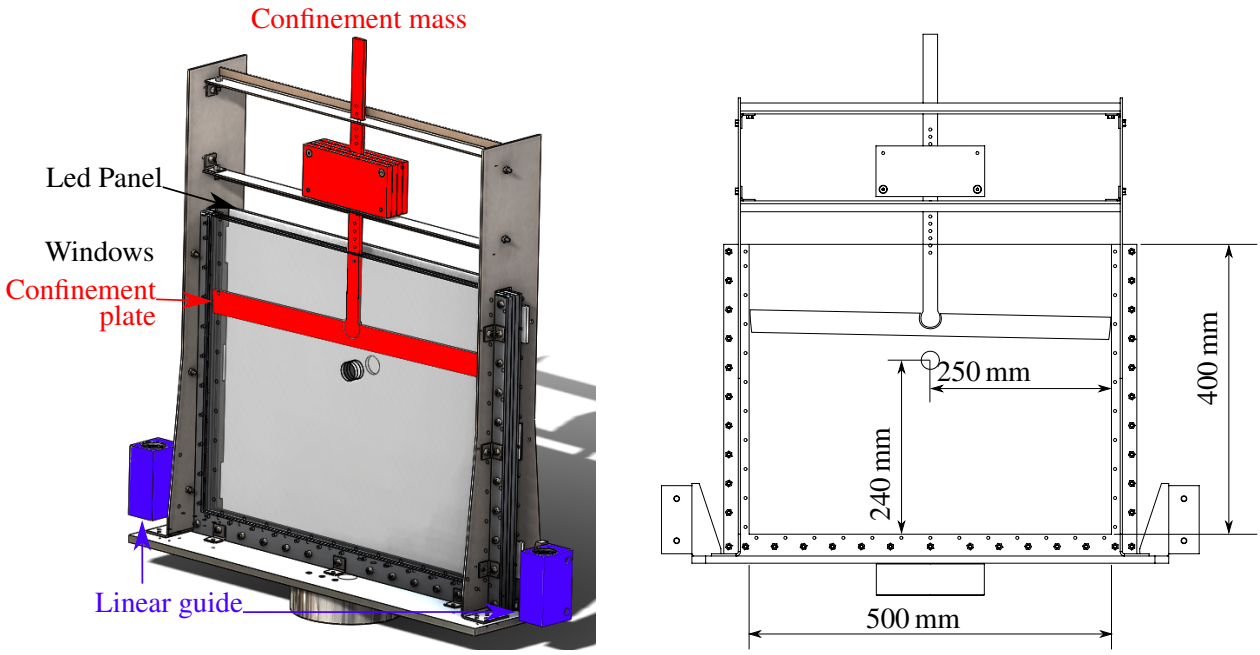

(a) 3D rendering

(b) Front view and dimensions

Fig. 9: Sketches of the vibrating frame

3.3 Vibrating frame

The goals of this device (Fig 9) are firstly to restrict the motion of the particles in a plane and secondly to transmit a vertical vibration to the granular media. The transmitted vibration motion is imposed by an hydraulic actuator, a `MTS` actuator model 204.52, of nominal force 2.5 t. The shape of the vertical motion is a sinusoidal with selected amplitude and frequency.

The successive element of the vibrating frame from back to front are:

1. a LED panel, to illuminate our granular media;
2. a left handed circular polarizer, to get circularly polarized light;
3. two windows spaced about 6 mm;
4. a confinement mass.

About the element of the polariscope (3.2.2), note that the led panel emits white light but the use of green particles limit the band of wavelength. As a consequence the visible dark fringes on the pictures can be computed for one wavelength. The circular polarizer is fixed on the windows as it is a thin flexible sheet. The analyzer is the final element of the polariscope which consists on a left-handed circular polarizer. It is fixed on the camera taking the pictures.

The windows separation is a compromise between two requirements. The first one is to avoid pressing and locking particles between the windows: this means to choose a value higher than the particles thickness. The second one requires as low space as possible between particles and windows to prevent the particles from slanting. We have chosen a distance of 6 mm between the 2 glasses because it will clearly never press particle; the ratio between the minimal particles diameter and this value is 2, and thus at worst, we preserve a contact of 4 mm between particles.

The last point concerning the windows is the drilled hole of diameter 25 mm through which passes the shaft transmitting the motion from the output bar of the four-bar linkage to the blender. As the four-bar linkage is ground fixed, this hole has to be sufficient to allow the vibration of the frame without inducing contact with the shaft, and small enough to avoid interfering with the particles.

The final element is a mass of 4 kg located between the two glasses in order to add a compaction or confinement load on the bed of particles (Fig 9a). This load is free to move vertically and a the plate in contact with the particles

can rotate between the windows. The center of mass of the rotating plate is on its center of rotation, and the moment of inertia is $42 \times 10^{-3}\,\mathrm{kg\,m^2}$. According to numerical simulations, this confinement load increases the differences in the length of the telescopic bar between different vibration frequencies. This load can be seen as if we add a lot of particles on the top of our experiment. But by doing so, our simulation would have been slower and our experiment would have been cumbersome.

On the left and right side of the vibrating box (Fig 9a) there are two linear guides. They prevent the box from rotating around the actuator axis and severely limit the rotation along the two other axis which are also fixed by the hydraulic actuator. The only one degree of freedom is thus the vertical vibration which is driven by the hydraulic actuator.

4 Results

The results are based either on the measure of the elongation of telescopic bar of the four-bar linkage (section 4.1) or on the pictures of the stress state inside the particles (section 4.2).

About the experimental process, the results were obtained with an imposed speed of the input bar of 15 rpm, an amplitude of vertical vibration fixed at 4 mm, but at several frequencies : 5, 8 and 10 Hz; each test lasts for 2 minutes. The same particles set (described in 3.2) is used for all the experiments. To avoid unwanted effects of loading history on the granular media in the results, each frequency is run multiple times in an random order regarding the other frequencies. Moreover, we have manually mixed and emptied the frame of all particles from time to time.

4.1 Four-bar linkage behavior

This section begin by presenting the experimental results obtained based on the four-bar linkage measures. Then the obtained numerical measure are introduced and discussed with regard to the experimental ones. To observe the resistance applied by granular media during the blending we measure the evolution of length of the telescopic bar. It could also be possible to measure the angular relative position between two bars of the linkage or even the torque applied by the motor. The length measure has been motivated by the the fact that the effect of the granular media was absorbed in this bar via the springs. Moreover a difference of angular position of the blender of 0.1° causes a change of length about 0.8 mm (exact value depends of base angle value), this length variation was more accessible to the sensor we had with regard to the available angular potentiometer. The measure of the motor torque was not considered as direct measured value as we do not include a torque sensor. The only way to retrieve the torque is based on current value and estimation of the motor parameters. This value is not directly comparable with numerical simulation.

The length of the telescopic bar during all the experiments is plotted at Fig 10. It represents a total of 9 experiments, each frequency was run 3 times but plotted with an unique color for the frequency. From these raws data, we already can observe that the amplitude of the length variation decreases while the excitation frequency increases, but the mean length of the telescopic bar seems to stay similar for all frequencies.

If we compute the fast Fourier transform of each experiment (Fig 11), we can observe the peaks corresponding to the motor frequency (f_{mot} =0.25 Hz) with some of its multiple and a smaller peak around the excitation frequencies (5, 8 and 10 Hz). It can also be seen that the amplitude of the first main harmonic is lowering as the excitation frequency increases. This confirms the observation done with the temporal evolution of the length. A closer look on these graphs shows a small difference between the applied frequency and the observed signal. By analyzing the hydraulic actuator motion, we found that it was unable to follow the frequency with the imposed amplitude of motion. Some modifications on the hydraulic setup and control will be investigate to see if we are able to follow the command.

To get some statistics on the amplitude of the telescopic bar, we have extracted the amplitude of motion at each motor cycle (Fig 12a) at each frequency. Then we can effectively see after some statistical treatment (Fig 12b) the influence of the excitation frequency on the response of the telescopic bar. As the excitation frequency increases, the mean amplitude decreases.

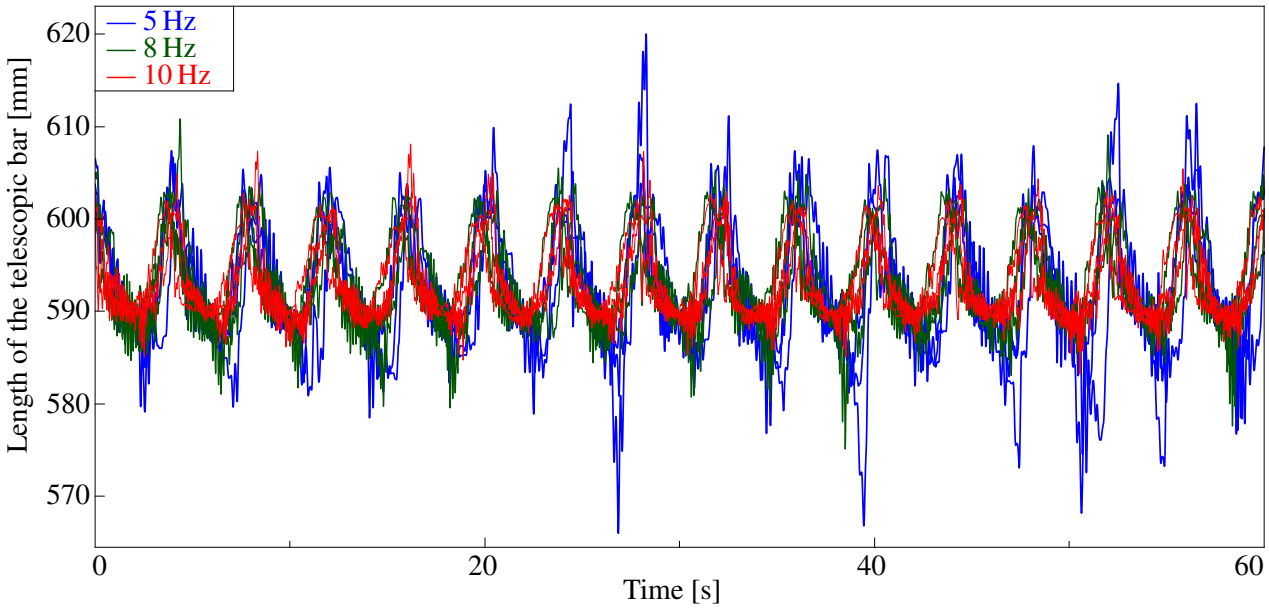

Fig. 10: Experimental results: Length of the telescopic bar during the experiments for all frequencies

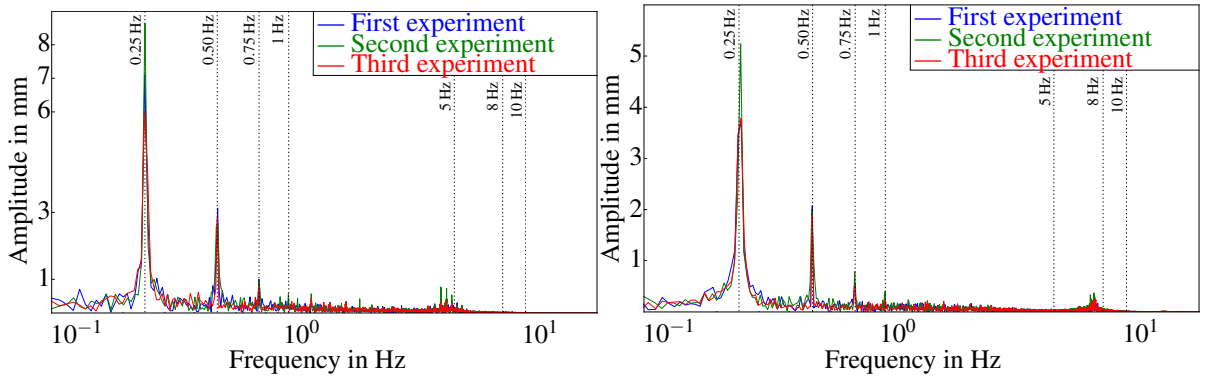

(a) External frequency: 5 Hz

(b) External frequency: 8 Hz

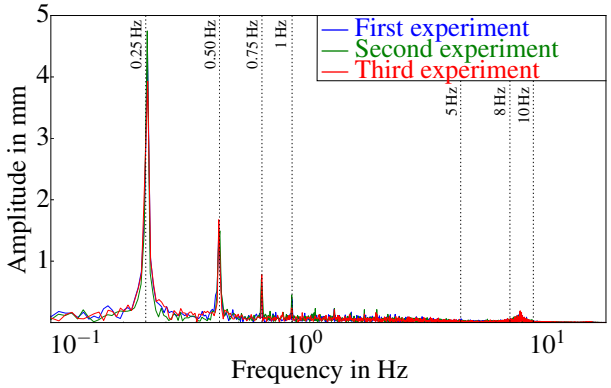

(c) External frequency: 10 Hz

Fig. 11: Experimental results: fast Fourier transform applied on the length of the telescopic bar

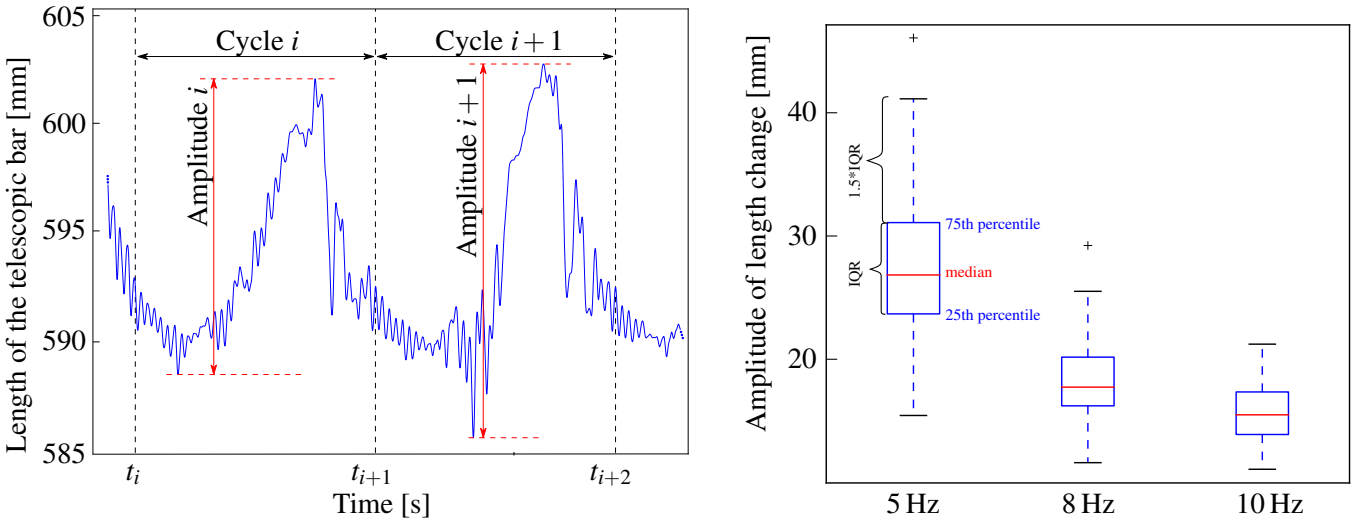

(a) Definition of the amplitude of a cycle

(b) Amplitude obtained for different excitation frequencies

Fig. 12: Experimental results: analysis of the amplitude of the length of the telescopic bar

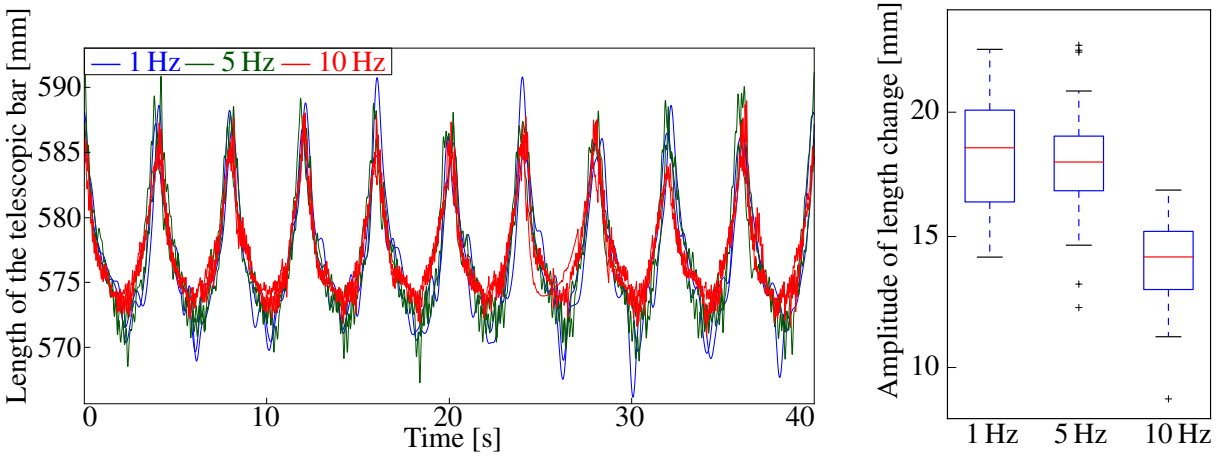

(a) Temporal evolution of the length

(b) Amplitude obtained for different excitation frequencies

Fig. 13: Numerical results: Length of the telescopic bar

4.1.1 Numerical results

The simulation results provides good trends. If we look at the length of the telescopic bar (Fig 13a), we also see a decreasing amplitude of the motion while the external vibration increases. This effect is more visible by the same analysis done on the motion amplitude (Fig 13b). However, the model still needs to be refined because one can clearly see by comparison with Fig 12b that the amplitude value differs as well as the value of decreasing amplitude, as the frequency increases.

The Fourier transform of the numerical signal (Fig 14) gives similar frequencies for the peaks. they are located at the motor frequency (0.25 Hz) with some of its multiples and also at the different excitation frequencies. Note that the simulated vibration corresponds to 1 Hz, 5 Hz and 10 Hz which differs from the set of experimental frequencies. Of course, the amplitude of the peaks differs from the experimental results. This is logical as the numerically obtained amplitudes of motion are lower than the experimental ones.

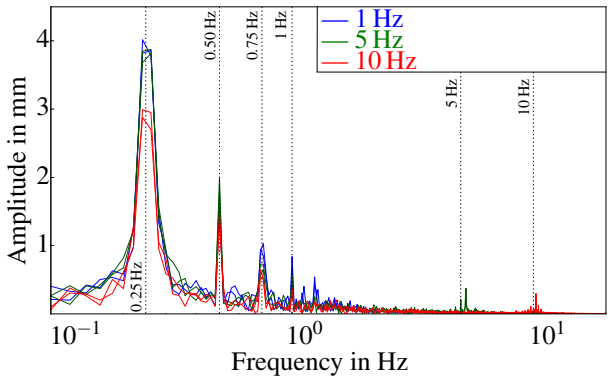

Fig. 14: Numerical results: Fast Fourier transform applied on the length of the telescopic bar

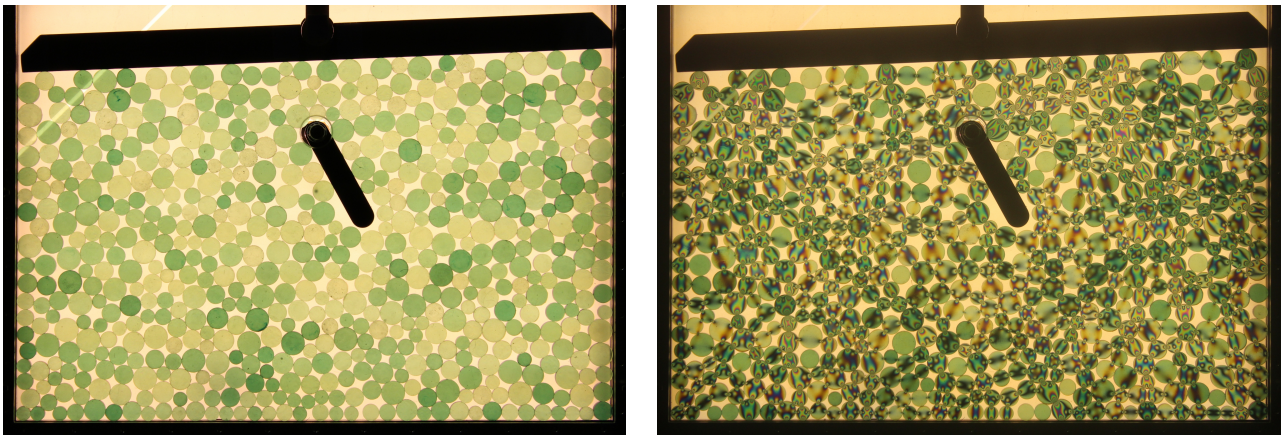

(a) Without polariscope

(b) With bright-field polariscope

Fig. 15: Pictures of the granular media in absence of motion

4.2 Granular media behavior

This section introduces the numerical treatment that will be done on the pictures of the granular stress states, and gives the first impression that we got. During the experiments, the camera recorded 1 frame by second showing the stress in the media; the Fig 15 shows the same state taken without and with the polariscope. This picture will be used in the remainder to explicit the numerical treatment that can be done. As the granular media has a chaotic motion, it will not be possible to numerically reproduce the exact same pictures (particles position, force network ...) of the granular media. However some trends should be reproducible in the numerical simulation.

The analysis of the granular media can be macroscopic or microscopic. The macroscopic ones are based on the change in compactness of the media, on the global motion of the particles, on average values computed on each particle. These treatments require to detect the particles position from the pictures, and eventually track them. After applying some treatments to the pictures (binarization...), the detection of particles position and diameter is done by functions based on the Hough transform. The interest of macroscopic observations lays in the fact that very few informations are needed. The only mandatory input is the pictures of the stress field in the granular media. The measures we do from these pictures are independent of the experiment parameters, although the gradient-squared method, explained below, can be improved by some calibration of the experiment.

On the opposite the microscopic observations require the determination of contact forces in the granular media, for such information the optical properties of the media is required. Then some typical informations are extracted from the forces value such as the mean force, the orientation of the strong forces network (forces larger than the mean value), or an averaged stress as defined by Weber [13].

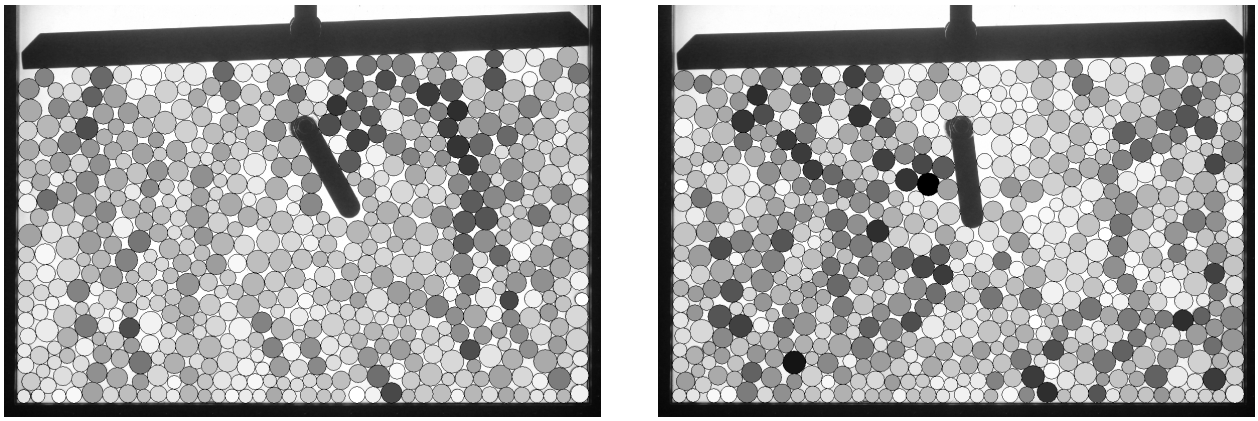

(a) Before experiment (b) After 2 minutes of blending

Fig. 16: Gradient-squared on particles, no vertical vibration

Compactness Obtaining the compactness of the media from the Fig 15b is immediate once the particles are detected. It will only consist in computing the ratio of particles surface over the area of a reference area. The evolution of this compactness can be compared between several point of view. It can be observe between the beginning and end of an experiment or during the motor cycle. The obtained evolution of compaction can then be compared with regards to the excitation frequencies. Both numerical and experimental measurement of the compactness can easily be obtained.

Gradient-squared method This measure also named G^2 is based on the number of dark/light fringes inside the granular media. As this number increase with the load on a particle, the gradient gives a semi-quantitative idea of the forces repartition inside the granular media. The measure is computed by

$$\langle G^2 \rangle = \sum_{i,j} \left[(I_{i+1,j} - I_{i-1,j})^2 + (I_{i,j+1} - I_{i,j-1})^2 + \frac{1}{2}(I_{i+1,j+1} - I_{i-1,j-1})^2 + \frac{1}{2}(I_{i+1,j-1} - I_{i-1,j+1})^2 \right] \tag{12}$$

where I is the light intensity, i and j denotes the index of the pixels belonging to the particle. The obtained value can be interpreted without any parameter related to the experiment. The result of such computation is given at Fig 16 where the G^2 has been computed on each particle before and after the experiment. Simple calibration allows to link the G^2 value to a pressure on the particle. As the numerical simulation computes the contact forces on each particles, we can easily compute an equivalent measure of the pressure on the particles.

By this macroscopic measure it is possible to compare some trends on the force repartition between frequencies and between numerical and experimental results. Does the force network creates horizontal or vertical chains of loaded particles? Does this behavior changes in function of the blender position?

Particles-velocity field While the evolution of compactness and force chains is important, it is also crucial to observe the shape of the particles-velocity field. This field characterizes the motion of the particles. Do they oscillate around a position? Do they circulate around the blender? What is the fraction, the area of moving particles? Is there a preferential motion direction? Do the results vary in function of the excitation frequency? An moreover do the numerical and experimental results match?

Determination of the forces in the granular media From the pictures of the stress state of the particles, it is possible to evaluate the forces inside the granular media. This evaluation required to express the stress field inside a particle submitted to arbitrary external forces and to know the value of C_λ, the stress-optic coefficient, of the material. A analytical solution of the stress field inside a cylindrical particle submitted to such load exists (see [14] and [15]). Knowing the stress field on each point of our particle, the retardation (δ) is computed by replacing the

principal stress values in the stress-optic law (eq 6). Then the intensity at each point of our particles is obtained by replacing δ in the equation 11. The needed input to this process are the locations, orientation and value of the contact forces.

The contact location on each particle can be determined from the picture once all particles have been located. The only unknowns, for each particle, are the force value and orientation. These values are computed by an optimization process applied to each particle. This process minimizes the difference between picture of the fringes of a particle and the analytical solution. The complete process is detailed by Daniel et al. [16] and their software is being adapted to our experiment.

Averaged stress The value of averaged stress in granular media proposed by Weber [13] on a reference cell is

$$\langle \sigma_S \rangle = \frac{1}{S} \sum_i (r_i \otimes d_i) \tag{13}$$

where S is the surface of the reference cell, i identify the contact belonging to the cell, r are the forces vector and d are the vectors joining the center of the grains in contact. The goal of this measure is to represent the granular media like a continuous media. The obtained experimental value can be compared with the numerical one in a similar way that was given for the gradient-squared method.

Strong forces network In a granular media, the forces network is not homogeneous. Some part of the particles are heavily loaded while other particle may be at rest. A common way to describe the forces in the granular media is to separate the network in 2. The forces larger than the mean value will constitute the strong network, while the other forces compose the weak network. Of course the first observation is the evolution of the force mean value. But once all forces are classified a typical study is to draw the orientation of the strong network. Again the evolution of the orientation can be studied during a typical motorcycle and then compared between frequencies. Looking for common trends between numerical and experimental measure is the final step of this analysis.

5 Conclusions and perspectives

In this paper we have presented an experimental benchmark that combines a multibody system in interaction with a granular media. The mechanical system is a four-bar linkage whose its floating rod has been replaced by a telescopic bar. All the necessary data have been provided to numerically reproduce the experiment with any numerical tools dedicated to this coupling problematic.

This experiment has been numerically reproduced by the methodology we developed that combines a multi-body formalism based on the coordinate partitioning method (to solve the bilateral constraints) and the non-smooth contact dynamics. Both experimental and numerical results were given. The first ones highlight the same trends in the behavior of the four-bar linkage between experimentation and simulation. However the obtained amplitude of motion was clearly not the same.

The simulations were conducted under some strong assumptions that need to be challenged. The strongest ones that will be investigate in the next future are related to the friction coefficient estimation and the rigidity of the particles. The assumption about the friction coefficient in the granular media can easily be relaxed. For now, a value of 0.6 has been arbitrarily imposed. A lower value is expected and could reduce the resistance on the blender motion and then increases the amplitude measured.

In our simulations, the granular media is considered as infinitely rigid, while in reality it is not. According the the Gent's relation a shore hardness of 95 A correspond to an approximative Young modulus of 43 MPa which is far from rigidity with regards to the involved forces. To relax this assumption, it may be possible to study the impact of some flexibility in the granular media. This flexibility can be studied by introducing, in the discrete element method, flexible grains (modeled by finite element method) or by replacing the contact law by a regularized one. Both solution can be realized in our tool. It may also be possible to replace particles in the experiment by harder

one, for example in metal; this will drastically reduce flexibility in the granular media but will unfortunately prevent any photoelastic study.

Finally the physical characteristics of our mechanism should be measured. For now almost all data's come from the numerical representation of our parts or from technical data sheets. Even if the measures done on some parts of the experimental set-up match the computed measures, the exact masses, inertias, centers of mass should ideally be confirmed by measure. Moreover the relation between the length of the telescopic bar and the force of the springs assembly need to be measured as well as the friction losses that should be evaluated.

To conclude, even if the current numerical results does not quantitatively match the experimental observations, these first results and the observed trends make us confident in our coupling strategy, that should converge toward the experimental results, if we relax above mentionned the assumptions in our further investigations.

Acknowledgements

This work is supported by a FRIA grant from the Fonds National de la Recherche Scientifique (FNRS) of Belgium and by the Wallonia.

References

[1] P. Flores, R. Leine, and C. Glocker, "Modeling and analysis of planar rigid multibody systems with translational clearance joints based on the non-smooth dynamics approach," *Multibody System Dynamics*, vol. 23, no. 2, pp. 165–190, 2010.

[2] M. Jean, "The non-smooth contact dynamics method," *Computer Methods in Applied Mechanics and Engineering*, vol. 177, no. 3, pp. 235–257, 1999.

[3] V. Acary and B. Brogliato, *Numerical Methods for Nonsmooth Dynamical Systems*, vol. 35 of *Lecture Notes in Applied and Computational Mechanics*. Berlin, Heidelberg: Springer Berlin Heidelberg, 2008.

[4] O. Brüls, V. Acary, and A. Cardona, "Simultaneous enforcement of constraints at position and velocity levels in the nonsmooth generalized-α scheme," *Computer Methods in Applied Mechanics and Engineering*, vol. 281, pp. 131–161, 2014.

[5] O. Lantsoght, P. Fisette, F. Dubois, O. Brüls, and N. Docquier, "Coupling multibody system and granular dynamics application to a 2D benchmark," vol. 140, p. 16007, 01 2017.

[6] R. A. Wehage and E. J. Haug, "Generalized Coordinate Partitioning for Dimension Reduction in Analysis of Constrained Dynamic Systems," *Journal of Mechanical Design*, vol. 104, pp. 247–255, Jan. 1982.

[7] F. Pfeiffer and C. Glocker, *Multibody Dynamics with Unilateral Contacts*. John Wiley & Sons, July 1996.

[8] J.-C. Samin and P. Fisette, *Symbolic Modeling of Multibody Systems*, vol. 112 of *Solid Mechanics and Its Applications*. Dordrecht: Springer Netherlands, 2003.

[9] N. Docquier, A. Poncelet, and P. Fisette, "Robotran: a powerful symbolic gnerator of multibody models," *Mechanical Sciences*, vol. 4, no. 1, pp. 199–219, 2013.

[10] O. Lantsoght, P. Fisette, F. Dubois, O. Brüls, and N. Docquier, "Coupling multibody and granular dynamics: application to a 2D benchmark," in *IMSD2016, The Fourth Joint International Conference on Multibody System Dynamics*, May 29 – June 2, Montral, Qubec, Canada 2016.

[11] K. Ramesh, *Digital Photoelasticity: Advanced Techniques and Applications*. Berlin Heidelberg: Springer-Verlag, 2000.

[12] R. C. Jones, "A New Calculus for the Treatment of Optical SystemsI. Description and Discussion of the Calculus," *JOSA*, vol. 31, pp. 488–493, July 1941.

[13] J. Weber, "Recherches concernant les contraintes intergranulaires dans les milieux pulvérulents : Application aux lois de similitude dans les études sur modèles réduits de problèmes de mécanique des sols pulvérulents," *Bulletin de liaison des Laboratoires Routiers*, vol. 20, 1966.

[14] S. P. Timoshenko, J. N. Goodier, and H. Norman Abramson, "Theory of Elasticity (3rd ed.)," *Journal of Applied Mechanics*, vol. 37, Jan. 1970.

[15] J. Michell, "Elementary distributions of plane stress," *Proc. London Math. Soc.*, vol. 32, pp. 35–61, 1900.

[16] K. E. Daniels, J. E. Kollmer, and J. G. Puckett, "Photoelastic force measurements in granular materials," *Review of Scientific Instruments*, vol. 88, p. 051808, May 2017.